Materials Today xxx (xxxx) xxx

Contents lists available at ScienceDirect

Materials Today

journal homepage: www.elsevier.com/locate/mattod

Research

Light-triggered multiphysics-coupled schottky superstructure for electrical stimulation and cell differentiation prediction with AI

Jianying Ji [a,b], Jiaxuan Li [b], Cong Liu [b,*], Yiqian Wang [a,b], Yuan Xi [b,e], Engui Wang [b,f], Yijie Fan [b], Yizhu Shan [b], Lingling Xu [b,f], Yuan Bai [a,b], Xi Cui [b,g], Longfei Li [b], Dan Luo [a,b,*], Zhou Li [a,b,c,d,*]

[a] Center on Nanoenergy Research, School of Physical Science & Technology, Guangxi University, Nanning 530004, China
[b] Beijing Institute of Nanoenergy and Nanosystems, Chinese Academy of Sciences, Beijing 101400, China
[c] Beijing Tsinghua Changgung Hospital, School of Clinical Medicine, Tsinghua University, Beijing 100084, China
[d] School of Biomedical Engineering, Tsinghua University, Beijing 100084, China
[e] Beijing Advanced Innovation Centre for Biomedical Engineering, Key Laboratory for Biomechanics and Mechanobiology of Ministry of Education, School of Biological Science and Medical Engineering, School of Engineering Medicine, Beihang University, Beijing 100191, China
[f] School of Nanoscience and Engineering, University of Chinese Academy of Sciences, Beijing 100049, China
[g] School of Biomedical Engineering Shenzhen Campus of Sun Yat-Sen University Shenzhen, 518107, China

ARTICLE INFO

Keywords:
Schottky superstructure
Multiphysics coupling
Light-trigger
Electrical stimulation
Real-time monitoring

ABSTRACT

Piezoelectric materials show unique potential in electrical stimulation therapy; however, their application faces two challenges: the cell-material interfaces are susceptible to perturbations by ultrasonic excitation; and there is a lack of effective strategies to dynamically monitor cellular feedback to electrical stimulation. Inspired by the optical-mechanical-electric coupling effect at the Schottky junctions, a light-triggered multi-physics coupled Schottky superstructure (LtMPc-SS) was prepared by binary self-assembly of barium titanate nanoparticles and gold nanorods. Under the synergistic effect of optomechanical coupling-induced piezoelectric polarization and Schottky energy barriers, LtMPc-SS generated free holes to electrically stimulate mesenchymal stem cells differentiation. Meanwhile, photoexcitation promoted the surface plasmon resonance of LtMPc-SS and realized the real-time detection of biomarkers based on surface-enhanced Raman scattering. The association between Raman spectra and cell differentiation status were established through artificial intelligence, enabling dynamic prediction of cellular differentiation progression. This study promises to usher in a new era of intelligent on-demand electrical stimulation.

Introduction

Life has existed in a variety of physical fields since its birth, and its occurrence and development process are affected by a variety of physical signals. The mutual coordination and transformation between different physical fields have a certain regulatory effect on cell division and differentiation [1,2]. As an important physical therapy strategy, electrical stimulation has shown significant application potential in the field of tissue engineering [3–11]. Studies have shown that electrical stimulation can effectively regulate stem cell proliferation and differentiation behavior, and has unique advantages in the regeneration of tissues such as bones [12,13], nerves [14], cardiovascular [15] and skin [16]. Due to the unique mechanical-electric coupling characteristics, piezoelectric materials have attracted much attention: this type of smart material can generate electrical signals through micromechanical deformation and directly act on the loaded cells, which provides a passive and convenient electrical stimulation pathway, showing unique advantages in the field of biotherapy [17–22]. Although piezoelectric materials have made significant progress in the field of tissue engineering [23,24], there are still two key problems that need to be solved. From the perspective of materials, the excitation of piezoelectric materials usually relies on local ultrasonic stimulation, which induces material deformation through cavitation effect and direct mechanical force. However, it is worth noting that while ultrasound promotes the generation of piezoelectric signals in materials, it also interferes with the cell-material interface, resulting in abnormal adhesion of stem cells and

* Corresponding authors at: Beijing Tsinghua Changgung Hospital, School of Clinical Medicine, Tsinghua University, Beijing 100084, China.
E-mail addresses: liucong@binn.cas.cn (C. Liu), luodan@binn.cas.cn (D. Luo), li_zhou@tsinghua.edu.cn (Z. Li).

https://doi.org/10.1016/j.mattod.2025.08.003
Received 27 April 2025; Received in revised form 25 June 2025; Accepted 3 August 2025

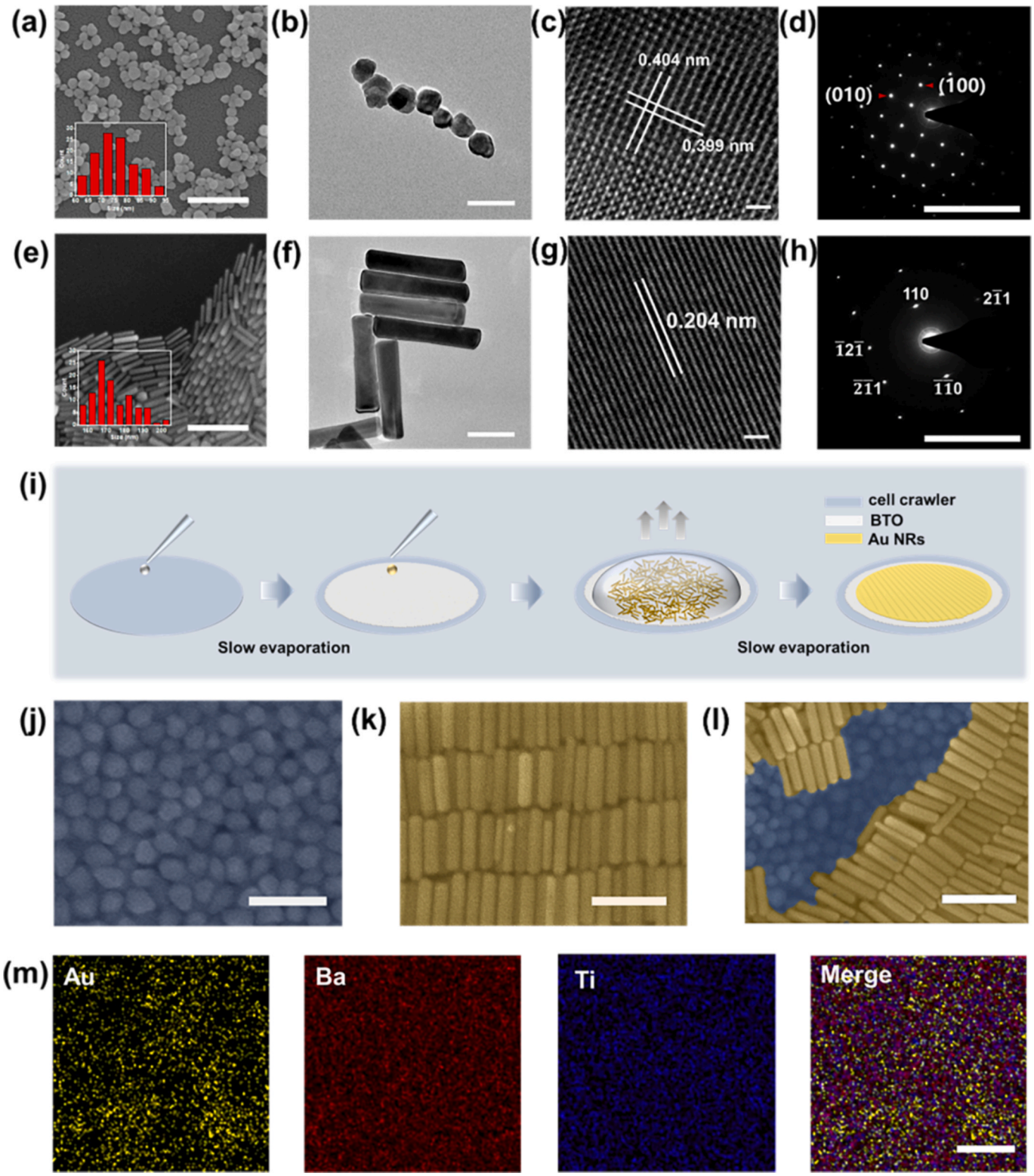

Fig. 1. Preparation and characterization of LtMPc-SS. (**a**) SEM image, (**b**) TEM image, (**c**) HRTEM image and (**d**) FFT image of BTO, the inset in Fig. 1A shows the particle size statistics of BTO. (**e**) SEM image, (**f**) TEM image, (**g**) HRTEM image and (**h**) FFT image of Au NRs, the inset in Fig. 1E shows the length statistics of Au NRs. (**i**) Schematic flow diagram of the preparation of electroactive substrates. (**j**) SEM image of the self-assembled BTO substrate. (**k**) SEM of the self-assembled Au NRs on LtMPc-SS. (**l**) SEM image of the self-assembled Au NRs on the surface of LtMPc-SS following disruption. (**m**) EDS mapping of LtMPc-SS. Scale bar: a, e = 250 nm; b, f = 100 nm; c, g = 1 nm; d, h = 10 1/nm, j, k = 150 nm, l = 200 nm and m = 100 nm.

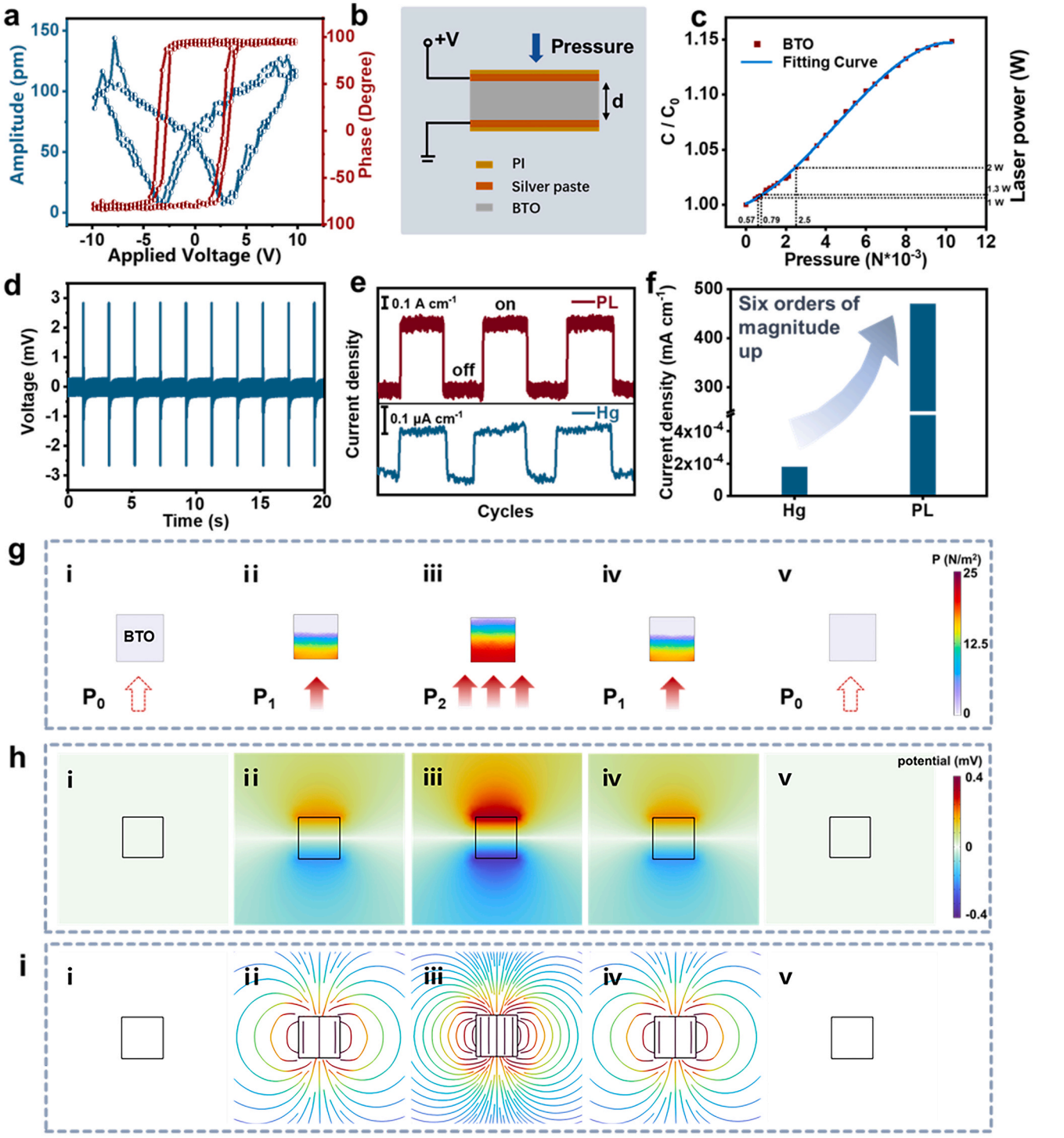

Fig. 2. Optomechanically-triggered piezoelectricity of BTO. (**a**) Piezoresponsive amplitude curve and phase curve of BTO nanoparticles. (**b**) Schematic representation of the BTO-based capacitive sensor. (**c**) Sensitivity curves of capacitive tactile sensors based on the BTO dielectric layer and the corresponding pressures of different laser powers. (**d**) Excitation response signal diagram of BTO under the pulsed laser pressure. (**e**) Photocurrent density of BTO under PL and Hg lamps. (**f**) Photocurrent density statistics of BTO under PL and Hg lamps. FEM simulations of optomechanically-triggered piezoelectricity of BTO using COMSOL Multiphysics software: (**g**) pressure, (**h**) piezoelectric potential distribution, and (**i**) electric field distribution.

even cell damage. From a biological perspective, existing technologies are difficult to achieve dynamic monitoring of cell differentiation status during piezoelectric stimulation, making the optimization of stimulation parameters mainly dependent on empirical adjustments, which seriously restricts the maximum therapeutic effect of piezoelectric stimulation. This dilemma emphasizes the importance of developing a piezoelectric composite platform that can generate piezoelectric stimuli without ultrasonic excitation, while taking into account real-time feedback on the state of cell differentiation.

Light irradiation is an ideal energy input method due to their high energy density and spatiotemporal controllability [25–27]. Specific wavelength laser light can not only excite the semiconductor material to produce electron-hole pairs, but also play its particle nature to produce pulsed radiation pressure, this photomechanical force induces

deformation and polarization of the piezoelectric material, thus realizing the light-triggered optical-mechanical-electric coupling. Compared with ultrasonic stimulation, light irradiation has the characteristics of high monochromaticity, collimated propagation characteristics and wide dynamic range of intensity, making light excitation more accurate and controllable with higher efficiency [28–36]. More importantly, light stimulation is friendly to the cell-material interface, avoiding problems such as cell detachment from the material surface and cell damage. In addition, it is worth pointing out that the absorption and scattering properties of light can accurately resolve the structure and abundance information of biomolecules. Raman spectroscopy, as a label-free analytical method, can rapidly obtain information of intracellular biomolecules with different polarizability by detecting inelastically scattered photons [37]. It can be seen that light irradiation can not only generate radiation pressure to excite piezoelectric materials; it can also track the dynamic expression of key differentiation-related markers through in-situ Raman fingerprint spectroscopy, thereby realizing real-time monitoring of the differentiation status of stem cells [38–41].

Inspired by this, we fabricated LtMPc-SS integrating stimulation and detection through the binary self-assembly of barium titanate nanoparticles (BTO NPs) and gold nanorods (Au NRs). When the pulsed laser (PL) irradiates the BTO NPs self-assembled at the bottom of LtMPc-SS from bottom to top, the radiation pressure induces the polarization of BTO NPs, generating a built-in piezoelectric field. The piezoelectric field causes the BTO band edge at the Schottky junction interface to bend downward, lowering the Schottky energy barrier, thereby promoting the directional migration of electrons from Au to the BTO conduction band. Under the synergistic effect of piezoelectric polarization triggered by opto-mechanical coupling and Schottky energy barriers, LtMPc-SS generates a large number of free holes to electrically stimulate mesenchymal stem cells loaded on the LtMPc-SS surface [9]. Moreover, the Au NRs self-assembled film on the upper layer of LtMPc-SS forms “hot spots” with strong local electromagnetic field at the gap between the assembled units through surface plasmon resonance (SPR), thereby greatly amplifying the surface-enhanced Raman scattering (SERS) signal and realizing the accurate detection of biomarkers in living cells. In recent years, the introduction of artificial intelligence (AI), especially machine learning algorithms, has provided a new way to mine potential biological information in Raman spectra [42,43]. Taking immunofluorescence staining, which is commonly used to identify the degree of differentiation of stem cells, as a standard, machine learning split and trained the characteristics of Raman spectra, and successfully established the association between Raman spectra and immunofluorescence staining of stem cells with different degrees of differentiation, so as to achieve real-time prediction of the differentiation of stem cells. In this study, LtMPc-SS provide a new paradigm for building closed-loop control of smart biological systems.

Results and Discussion

Preparation and characterization of LtMPc-SS

BTO NPs were synthesized by hydrothermal method using barium nitrate and tetrabutyl titanate as precursors. As shown in Fig. 1a and Fig. 1b, scanning electron microscopy (SEM) and transmission electron microscopy (TEM) images reveal that the nanoparticles have an average size of approximately 77.5 ± 15 nm. High-resolution transmission electron microscopy (HRTEM) analysis (Fig. 1c) confirms that the synthesized BTO NPs exhibited a defect-free, single-crystal structure with facet spacings of 0.399 and 0.404 nm, corresponding to the (100) and (001) crystal planes, respectively. Meanwhile, selected area electron diffraction (SAED) corroborated the principal crystallographic orientation aligned along [001] (Fig. 1d). X-ray diffraction (XRD) characterization (Fig. S1) further identified peak splitting near $2\theta = 45^{\circ}$, which are consistent with distinct (002) and (200) reflections of the tetragonal piezoelectric structure of BTO, as referenced in the JCPDS database (no. 05–0626). Then, Au NRs were synthesized by a seed method using tetrahydrated chloroauric acid as starting material in a binary surfactant mixture consisting of cetyltrimethylammonium bromide (CTAB) and sodium oleate (NaOL) via a chemical process. SEM and TEM images show that Au NRs with the length of 175 ± 20 nm and the width of 77.5 ± 15 nm were successfully synthesized (Fig. 1e, Fig. 1f and Fig. S2). HRTEM analysis distinctly displays the lattice spacing of Au NRs is 0.204 nm, corresponding to the (200) crystal plane of cubic gold (Fig. 1g and Fig. 1h).

The fabrication of LtMPc-SS is depicted in Fig. 1i, which was self-assembled by slow solvent evaporation. The relatively weak attractions between nanocrystals effectively screened in solution become apparent as the solvent evaporates, triggering the assembly of complex, slowly evolving superstructures [44,45]. Here, self-assembling BTO NPs and Au NRs onto the glass substrate (cell slide) surface was conducted in two steps. Specifically, first, the dispersion of BTO NPs in water was transferred to a glass substrate, and the BTO NPs were uniformly attached to the glass substrate by controlling the evaporation rate of water (Fig. 1j). In order to remove ligand impurities on the surface of BTO NPs and effectively contact with Au NRs, the surface of the assembled BTO layer was treated with plasma. Next, the Au NRs were assembled on the BTO layer using the same method to obtain LtMPc-SS. To prove successful preparation, the morphology of LtMPc-SS was characterized by SEM (Fig. 1k), showing the uniform and ordered arrangement of the Au NRs layer achieved by self-assembly. After removing the Au NRs from the surface, the tightly packed BTO layer is exposed, as shown in Fig. 1l. In addition, STEM-coupled energy dispersive X-ray spectroscopy (EDS) mapping (Fig. 1m) confirmed the uniform distribution of BTO and Au on the surface of LtMPc-SS.

Optomechanically-triggered piezoelectricity of BTO

First, the piezoelectric properties of BTO were confirmed by piezoresponse force microscopy (PFM). As shown in Fig. 2a, the imposition of a ramp voltage ranging from −10 V to +10 V on BTO produces a characteristic butterfly-shaped curve, reflecting strain variations under an external electric field. In addition, the phase profile reveals localized piezoelectric hysteresis in BTO with a phase shift of approximately 180°, demonstrating robust polarization switching behavior. These findings confirm the exceptional piezoelectric properties of BTO. According to previous reports, pulsed laser could provide large light pressure [35]. Then, in order to systematically study the PL-triggered piezoelectricity, a miniature capacitive pressure sensor was developed using BTO to detect pressure induced by a 355 nm laser. A schematic representation of the BTO-based capacitive sensor is shown in Fig. 2b. The relationship between the rate of capacitance changes and external pressure was investigated by applying varying pressures to the BTO-based sensor, thus generating a standard pressure-response curve (Fig. 2c). The capacitance of sensor exhibits measurable changes upon laser beam impact on its surface. Capacitance measurements were conducted using laser powers of 1.0, 1.3, and 2.0 W, yielding corresponding pressures of 5.7×10^{-4}, 7.90×10^{-4}, and 2.50×10^{-3}N, respectively. These findings confirm that applying PL to the BTO surface generates measurable pressures. Specifically, the output signal corresponding to the pressure induced by pulsed laser is illustrated in Fig. 2d.

To further clarify the PL-triggered piezoelectricity of BTO, photoelectric measurements were conducted to investigate deeper insights into the underlying processes. In the course of this test, both BTO and TiO_2 have significant absorption in the UV region (Fig. S3), indicating that they can be excited by PL and Hg lamps at 355 nm. Therefore, TiO_2 was chose as a control group in the photoelectrochemical measurement experiments. As shown in Fig. 2e and Fig. 2f, the photocurrent density of BTO under Hg lamp irradiation is 0.0018 μA cm^{-2}, while the photocurrent density under PL irradiation is 0.47 A cm^{-2}, an increase of six orders of magnitude. For TiO_2, as shown in Fig. S4, the photocurrent

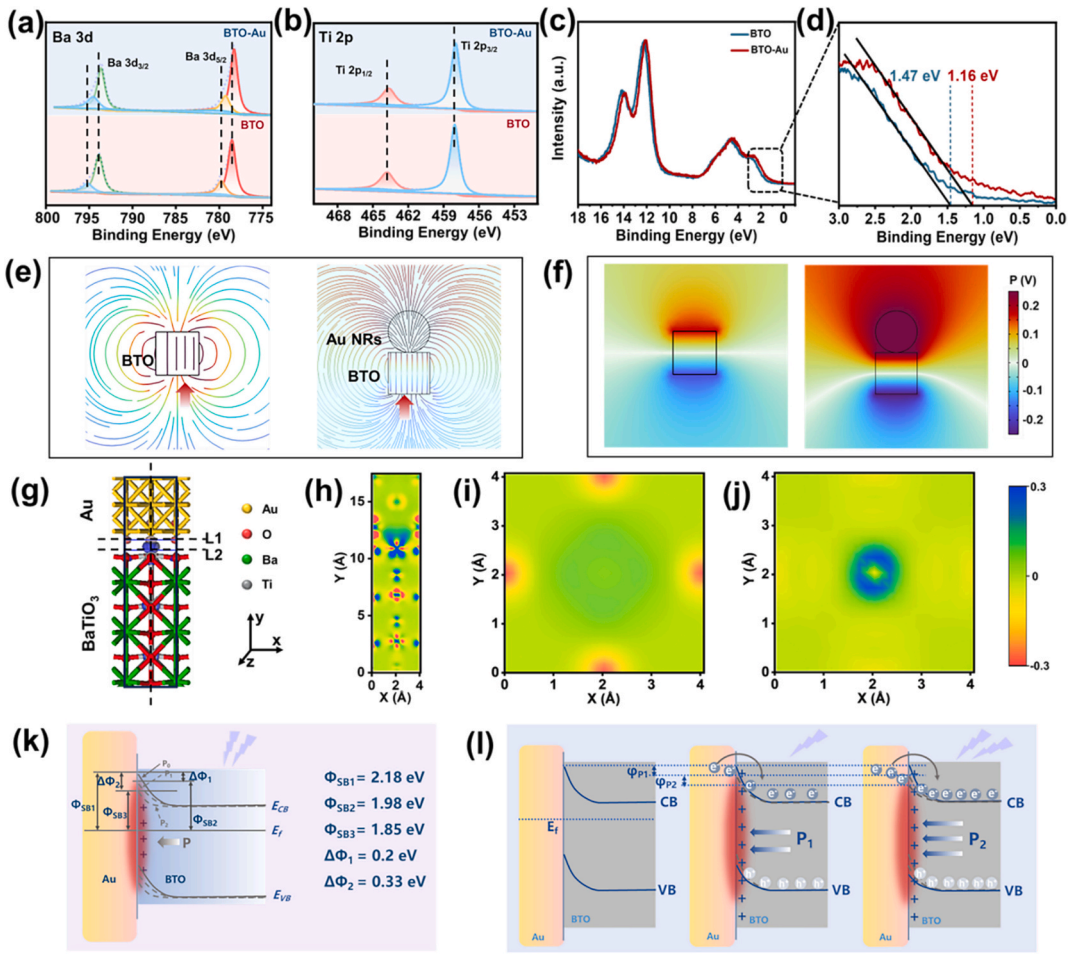

Fig. 3. Mechanism analysis of enhanced polarization potential in LtMPc-SS. High resolution XPS spectra of (**a**) Ba 3d and (**b**) Ti 2p in pure BTO and BTO-Au NRs. (**c**) and (**d**) valence band XPS analysis of BTO and BTO-Au. FEM simulations of dynamic laser-triggered piezoelectricity using COMSOL Multiphysics software: (**e**) electric field distribution and (**f**) piezoelectric potential distribution. (**g**) Atomic structure model of BTO-Au. Sectional view of charge density distribution of BTO-Au slicing along y (**h**), x-L1 (**i**) and x-L2 (**j**). (**k**) Schottky barrier of BTO-Au under various applied stress. (**l**) Schematic diagram of mechanism analysis of enhanced polarization potential in BTO-Au under applied stress.

densities under Hg lamp and PL are 0.019 μA cm^{-2} and 0.21 A cm^{-2}, respectively. Due to the superior intrinsic photoelectric properties of TiO_2, the photocurrent density of TiO_2 is significantly higher than that of BTO under Hg lamp irradiation. In contrast, under PL excitation at 355 nm, both BTO and TiO_2 demonstrated a pronounced enhancement in photocurrent response. Notably, the photocurrent produced by BTO under PL excitation significantly exceeds that of TiO_2, providing indirect evidence for PL-triggered piezoelectricity of BTO.

Laser radiation exhibits wave-particle duality. As electromagnetic radiation, it propagates as waves, while its constituent photons carry momentum. According to principles derived from both classical electrodynamics and quantum mechanics, when a light beam interacts with a material surface (via absorption, reflection, or refraction), it exerts radiation pressure on the object due to momentum transfer. Specifically, each photon carries momentum: $p = h / \lambda$. Where h is Planck's constant and λ is the wavelength. When the laser irradiates the material surface, the photons transfer their momentum through absorption, scattering, or reflection. [46].

To elucidate the potential generated by PL-induced piezoelectricity of BTO, finite element method (FEM) simulations were conducted using COMSOL software to model potential variations and electric field distributions within BTO under light pressure. As shown in Fig. 2g, five distinct light-pressure states were analyzed: no laser irradiation (P_0), initial laser pressure (P_1), elevated laser pressure (P_2), reduced laser pressure to P_1, and complete withdrawal of laser pressure (P_0). Applying laser pressure to P_1 induces piezoelectric potential and an intrinsic electric field, attributed to the deformation of BTO (Fig. 2g-ii). At the maximum applied pressure ($P_2 = 25$ N/m^2), the piezoelectric potential (Fig. 2h-iii) and the intrinsic electric field (Fig. 2i-iii) reach their peak values. Upon the cessation of laser pressure from P_2 to P_1 and P_0, the deformation of BTO is reversed, accompanied by the recovery of piezoelectric potential and the electric field.

Mechanism analysis of enhanced polarization potential in LtMPc-SS

To elucidate the underlying mechanism of enhanced polarization potential in LtMPc-SS, we first employed X-ray photoelectron spectroscopy (XPS) to investigate the carrier transport dynamics within the material system. As demonstrated in Fig. 3a-3b and S5, the high-resolution XPS spectra of BTO show a clear shift in the binding energy of Ba 3d, Ti 2p, and O 1s, suggesting that the interaction of BTO and Au is more than just physical contact. Specifically, as shown in Fig. 3a, compared with BTO alone, the binding energy of Ba $3d_{3/2}$ in BTO-Au is reduced from 795.2 eV and 793.9 eV to 794.5 eV and 793.6 eV, respectively; the binding energy of Ba $3d_{5/2}$ configuration is reduced from 779.7 eV and 778.5 eV to 779.3 eV and 778.3 eV, respectively. The binding energy of Ti $2p_{1/2}$ is reduced from 458.05 eV to 457.9 eV; the binding energy of Ti $2p_{3/2}$ is reduced from 463.78 eV to 463.66 eV (Fig. 3b). The binding energy of O 1s is reduced from 529.45 eV to 529.1 eV (Fig. S5). Upon coupling of BTO with Au, Ba 3d, Ti 2p and O 1s are all

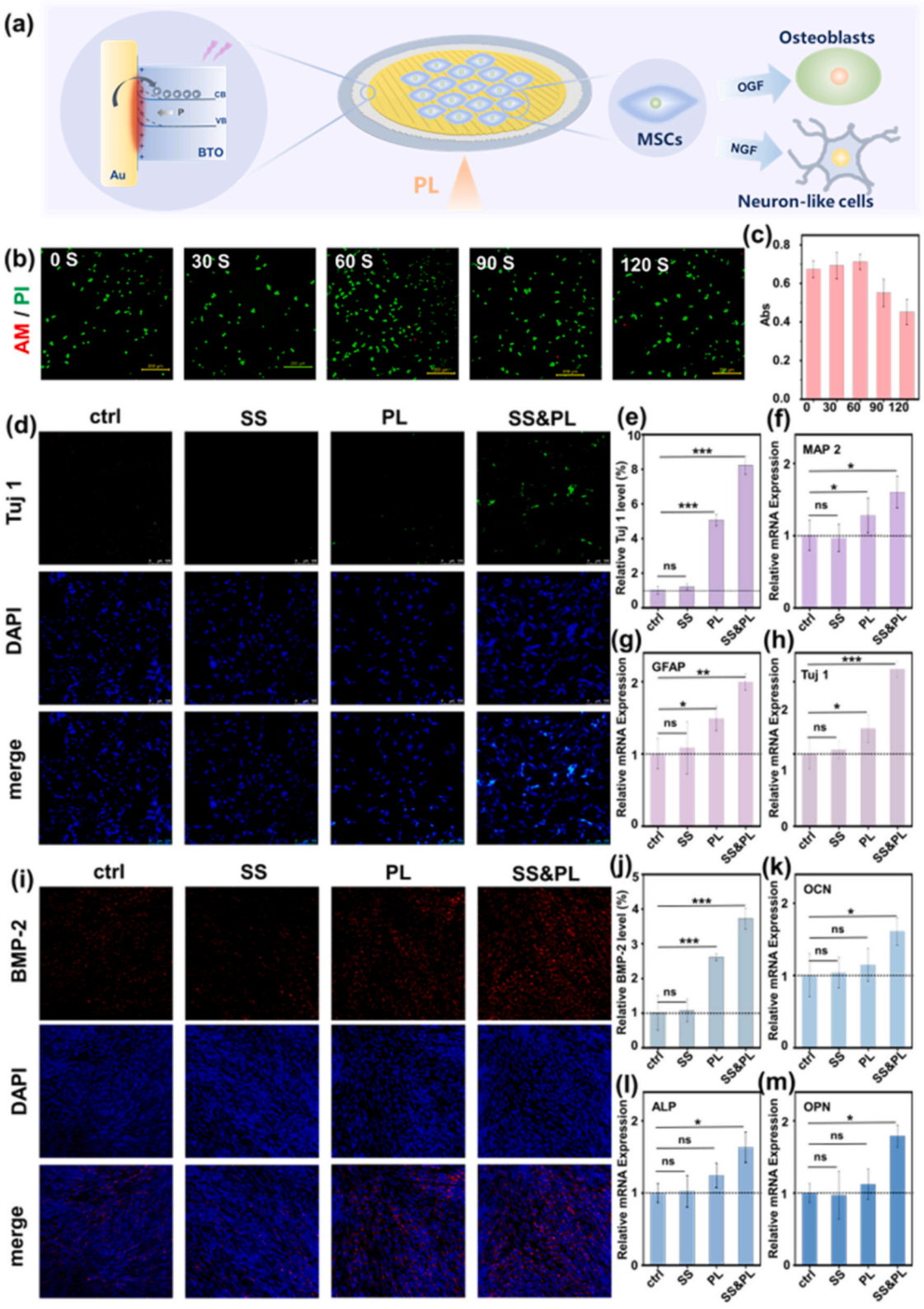

Fig. 4. Optomechanically-triggered electrical stimulation of cell differentiation. (**a**) Schematic representation of applying pulsed laser-triggered piezoelectric potential to promote MSCs differentiation to neuron-like cells or osteoblasts. (**b**) Live-dead staining of MSC after pulsed laser stimulation at different times. (**c**) CCK-8 of cells at different stimulation times following 72 h of culture. Immunofluorescence staining of (**d**) neuron-specific maker Tuj-1 and (**i**) osteoblast-specific maker BMP-2. Statistical analysis of the fluorescence intensity of (**e**) Tuj-1 and (**j**) BMP-2 with ImageJ. Relative mRNA expression of (**f**) MAP 2, (**g**) GFAP, (**h**) Tuj-1, (**k**) OCN, (**l**) ALP and (**m**) OPN after MSCs neurogenesis for 7 days. Data were expressed as mean ± standard deviation (SD) (n = 3). Analyzed by one-way ANOVA, *P < 0.05, **P < 0.01, ***P < 0.001, ns P > 0.05.

shifted to low binding energy, indicating that BTO acts as an electron acceptor with the migration of electrons from Au to BTO. Generally, when a metal and semiconductor come into contact, the difference in their work functions allows electrons to flow from the metal to the semiconductor until their Fermi levels reach equilibrium, creating band bending in the semiconductor and establishing the Schottky barrier. Then, valence band XPS analysis was conducted on both pristine BTO and BTO-Au to verify the interfacial charge transfer dynamics and Schottky barrier formation between BTO and Au. As revealed in Fig. 3c and Fig. 3d, distinct shifts emerge in the valence band XPS spectra following Au integration. Quantitative analysis reveals the valence band maximum (VBM) positions at 1.47 eV for pristine BTO versus 1.16 eV for BTO-Au, namely, a 0.31 eV negative shift upon Au coupling, which is attributed to interfacial electron transfer from Au to BTO and establishment of Schottky barrier at the BTO-Au interface.

Subsequently, to assess the piezoelectric response under mechanical stimulation, FEM simulations were performed to model the potential variations and electric field distributions in pristine BTO and BTO-Au under light pressure. The computational results (Fig. 3e and Fig. 3f) reveal a pronounced enhancement in interfacial potential difference for the BTO-Au system compared to BTO, demonstrating superior charge separation efficiency of BTO-Au. Notably, the simulated potential distribution shows that the field intensity inside BTO-Au was amplified by 1.7 times, confirming that BTO-Au significantly amplifies the piezoelectric polarization.

To unravel the in-deep origin of the enhanced polarization potential in LtMPc-SS, we conducted systematic density functional theory (DFT) simulations focusing on charge carrier dynamics. As depicted in Fig. 3g-3j, first-principles calculations reveal substantial interfacial charge redistribution within the BTO-Au interface. Specifically, charge density distribution of BTO-Au exhibits pronounced interfacial charge polarization, with distinct electron accumulation (blue regions) and depletion (red regions) at the interfacial zone. The observed asymmetric distribution of charge directly correlates with the Schottky barrier modulation identified in valence band XPS, where electron transfer from Au to BTO induces a downward shift in the valence band maximum. Furthermore, the effect of various applied stress on Schottky barrier at metal–semiconductor interfaces was investigated using DFT calculations. As dynamically illustrated in Fig. 3k and Fig. S6, the applied mechanical stress (P1) induces a characteristic 0.2 eV downward band bending at the BTO interface ($\Delta\Phi1$), effectively reducing the Schottky barrier from the initial 2.18 eV (Φ_{SB1}) to 1.98 eV (Φ_{SB2}). Subsequent stress intensification to P2 amplifies this piezoelectric polarization, generating an additional 0.13 eV downward band bending ($\Delta\Phi_2$ - $\Delta\Phi_1$= 0.13 eV), then further lowering the Schottky barrier to 1.85 eV (Φ_{SB3}).

Combining the above experimental results with calculation data, mechanism analysis of enhanced polarization potential in BTO-Au under applied stress is depicted in Fig. 3l. Under continuous pulsed laser irradiation, the optical pressure persistently polarizes the BTO NPs, inducing interfacial band bending that reduces the Schottky barrier compared to the static state. Then, the reduction of the Schottky barrier creates a favorable environment for electrons to flow from Au to BTO. Under the synergistic effect of piezoelectric polarization of BTO triggered by opto-mechanical coupling and Schottky energy barriers, LtMPc-SS can generate a large number of free holes to electrically stimulate mesenchymal stem cells loaded on the LtMPc-SS surface.

Optomechanically-triggered electrical stimulation of cell differentiation

Existing studies have reported that electrical signals can regulate cell differentiation and proliferation [20,47–49]. Applying PL-triggered multiphysics-coupled Schottky superstructure to electrically stimulate mesenchymal stem cell (MSCs) differentiation to neural-like cells or osteoblasts was investigated as follows (Fig. 4a). To evaluate the influence of LtMPc-SS on cell proliferation, MSCs were initially incubated on tLtMPc-SS in a growth medium for 2 days, ensuring the establishment of five groups of cells with equivalent status. Following this initial period, LtMPc-SS with MSCs were exposed to intermittent PL irradiation daily for durations of 0, 30, 60, 90, and 120 s. Cell viability was assessed after 3 days using live/dead staining and CCK-8 assays. As shown in Fig. 4b, the proliferation of MSCs was maximized when subjected to daily intermittent PL irradiation for 60 s. However, when the stimulation period exceeded 60 s, a significant reduction in cell proliferation was observed, consistent with the trend of the CCK-8 assay results (Fig. 4c). Subsequently, MSCs were incubated on LtMPc-SS in a medium containing osteogenic growth factor (OGF) and neural growth factor (NGF). To evaluate the influence of LtMPc-SS and PL stimulation (abbreviatively, SS&PL) on the differentiation of MSCs into neuron-like cells, the expression of Tuj-1, a neuronal marker, was assessed via immunofluorescence staining (Fig. 4d and Fig. 4e). After 7 days of cultivation, cells grown on LtMPc-SS without PL stimulation exhibited negligible Tuj-1 expression. Similarly, cells cultured under standard conditions but subjected to PL stimulation displayed minimal Tuj-1 expression. In contrast, cells cultured on LtMPc-SS and exposed to daily PL stimulation showed significantly elevated Tuj-1 expression compared to the other groups, highlighting the synergistic effect of LtMPc-SS and PL stimulation in promoting neuronal differentiation. To further substantiate the influence of LtMPc-SS and PL stimulation on the neuron-like cells differentiation of MSCs at the genetic level, quantitative polymerase chain reaction (qPCR) was performed to assess the expression of key neural differentiation markers, including microtubule-associated protein 2 (MAP-2), glial fibrillary acidic protein (GFAP), and Tuj-1. Notably, cells cultured on LtMPc-SS with PL stimulation exhibited significantly elevated expression levels of MAP-2, GFAP, and Tuj-1 compared to other experimental groups (Fig. 4f-4h).

To evaluate the impact of LtMPc-SS and PL stimulation on the differentiation of MSCs into osteoblasts, BMP-2 expression, an osteoblast-specific maker, was assessed via immunofluorescence staining (Fig. 4i and Fig. 4j). After a 7-day culture period, BMP-2 expression was markedly elevated in cells cultured on LtMPc-SS with PL stimulation, compared to the other experimental groups. Alizarin Red S staining, a standard method for assessing osteogenic differentiation via the detection of mineralized nodules formed by cytosolic calcium secretion, was employed to further evaluate this process. As shown in Fig. S7, mineralized nodules were significantly increased in cells cultured on LtMPc-SS under PL stimulation compared with other groups. To further elucidate the influence of LtMPc-SS with PL stimulation on the osteogenic differentiation of MSCs at the genetic level, qPCR analysis was performed to quantify the mRNA expression levels of key osteogenic markers, including osteopontin (OPN), osteocalcin (OCN), alkaline phosphatase (ALP), and runt-related transcription factor 2 (Runx2). The expression levels of the four osteogenic markers following seven days of culture were presented. As validated in Fig. 4k-4m and Fig. S8, cells cultured on LtMPc-SS with PL stimulation exhibited significantly elevated expression levels of OCN, ALP, OPN, and Runx2 compared to other experimental groups. These findings collectively underscore the facilitating role of LtMPc-SS and PL stimulation in promoting the differentiation of MSCs into multiple lineages.

Furthermore, while ultrasound remains one of the most widely used methods for stimulating piezoelectric materials, it presents several challenges, such as cell detachment. In contrast, light stimulation effectively mitigates this issue. To evaluate this hypothesis, we compared the adhesion of cells subjected to the same stimulation duration (intermittent stimulation for 1 min). For better visualization, the nucleus and cytoskeleton were stained. As illustrated in Fig. S9, a significantly higher number of adherent cells were observed under pulsed-laser stimulation compared to ultrasound stimulation.

Real-time monitoring cell differentiation via SERS

The differentiation of MSCs into neural-like and osteoblastic lineages is associated with distinct alterations in their chemical profiles.

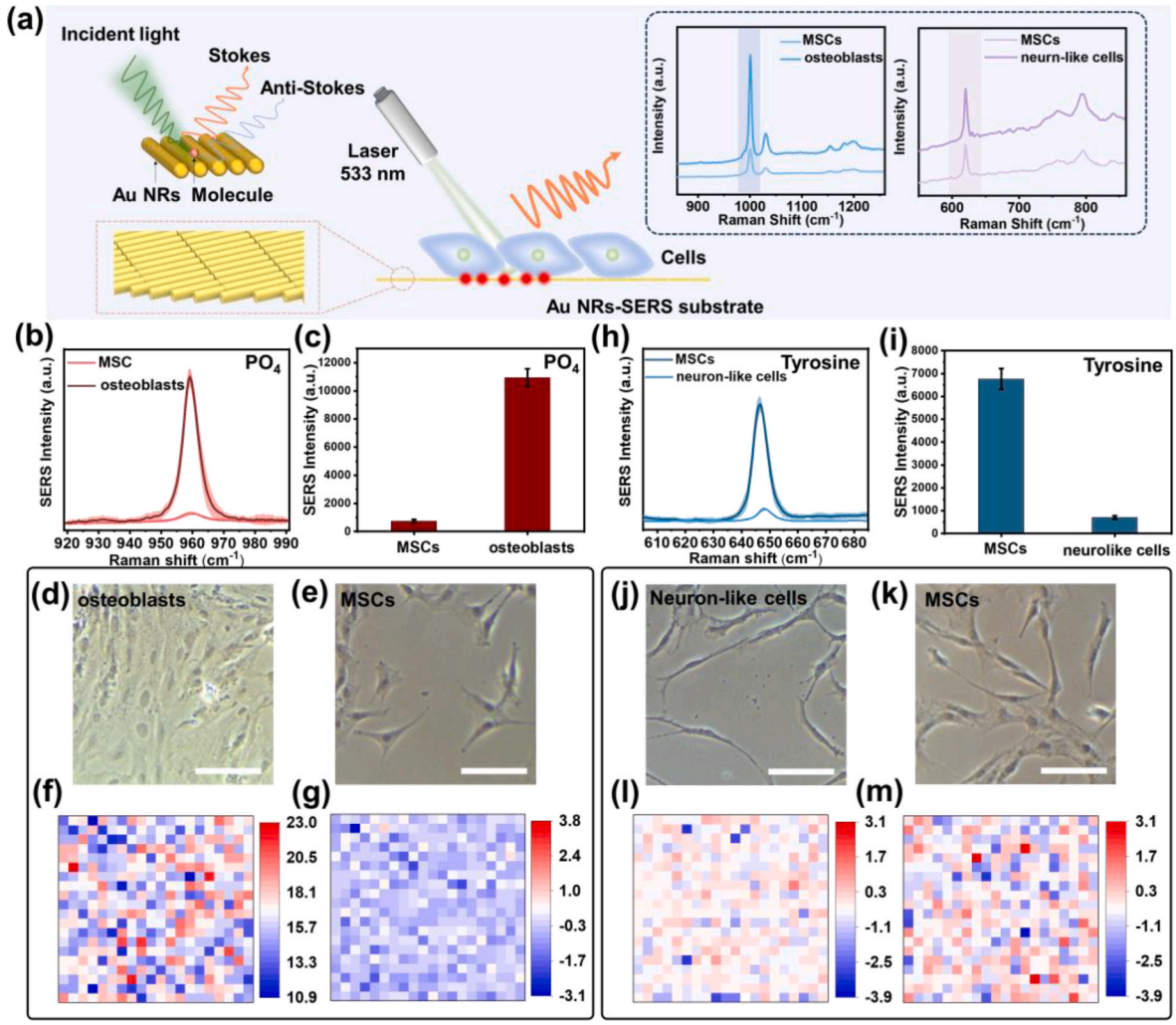

Fig. 5. Real-time monitoring cell differentiation via SERS. (**a**) Schematic representation of real-time monitoring cell differentiation via SERS. (**b**) SERS spectra of PO_4 in MSCs and osteoblast cells. (**c**) Statistical analysis of Raman intensity of PO_4 level in MSCs and osteoblasts. Micrographs of (**d**) MSCs and (**e**) osteoblast cells. SERS mapping of PO_4 signals on 10 × 10 μm^2 cell monolayers corresponding to (**g**) MSCs and (**f**) osteoblast cells. (**h**) SERS spectra of tyrosine in MSC and neuron-like cells. (**i**) Statistical analysis of Raman intensity of tyrosine level in MSCs and osteoblasts. Micrographs of (**k**) MSCs and (**j**) neuron-like cells. SERS mapping of tyrosine signals on 10 × 10 μm^2 cell monolayers corresponding to (**m**) MSCs and (**l**) neuron-like cells. Scale bar: d, e, j and k = 1 μm.

Specifically, neural-like cells exhibit a reduction in the amino acid tyrosine, whereas osteoblastic cells show an increase in phosphate levels [50,51]. Raman spectroscopy serves as a powerful tool for molecular fingerprinting, being able to provide detailed structural information of natural chemical components within the nucleus and cytoplasm, including DNA, RNA, phenylalanine, and other cellular molecules. However, a key limitation of this technique lies in its relatively low sensitivity, due to the inherently weak nature of Raman scattering. This challenge can be significantly mitigated via the self-assembled Au NRs with exceptional localized SPR, making them ideal candidates as substrates for SERS. Here, the self-assembled Au NRs were established on the piezoelectric substrate via slow evaporation strategy (Fig. 1i-1l). The schematic depiction of real-time monitoring cell-specific markers via SERS signal obtained from the self-assembled Au NRs is shown in Fig. 5a. Laser with a wavelength of 533 nm irradiates the self-assembled Au NRs on the upper layer of LtMPc-SS from above. SERS spectra of cell-specific markers were acquired by irradiating the cell surface with a focused spot size of 1 μm, covering an area of 10 × 10 μm^2. Notably, variations in the spectra derived from significant differences in the expression of specific biomolecules are typically attributed to the inherent heterogeneity of the cells. In particular, osteogenic differentiation and mineralization processes are associated with elevated phosphate levels. As illustrated in Fig. 5b, the characteristic peak of phosphate is prominently observed at approximately 960 cm^{-1} in the Raman spectra of MSCs and osteoblasts. The normalized signals for osteoblasts and MSCs are presented in Fig. 5c. The characteristic peak of phosphate at 960 cm^{-1} was showed through SERS imaging. These images illustrate the distribution of phosphate across a 10 × 10 μm^2 cell monolayer, corresponding to the data derived from Fig. 5d-5g, respectively. The results reveal that the phosphate level is significantly more pronounced in osteoblasts compared to MSCs.

In the process of MSC differentiation into neural-like cells, a characteristic Raman spectral change is observed, namely the gradual attenuation of the peak at 646 cm^{-1}, which corresponds to the vibrational mode of tyrosine. Thus, the Raman peak at 646 cm^{-1} can serve as a distinctive marker for differentiating between MSCs and neural-like cells (Fig. 5h). As shown in Fig. 5h-5i and Fig. 5j-5m, the normalized SERS mapping images for MSCs and neural-like cells at 646 cm^{-1} depict the spatial distribution of the cells across a monolayer of 10 × 10 μm^2. The results reveal that the vibrational mode of tyrosine in neural-like cells is significantly weakened compared to MSCs. On the whole, the characteristic peak of phosphate at 966 cm^{-1} and tyrosine at 646 cm^{-1} can serve as a distinctive marker for real-time monitoring MSCs differentiation via SERS.

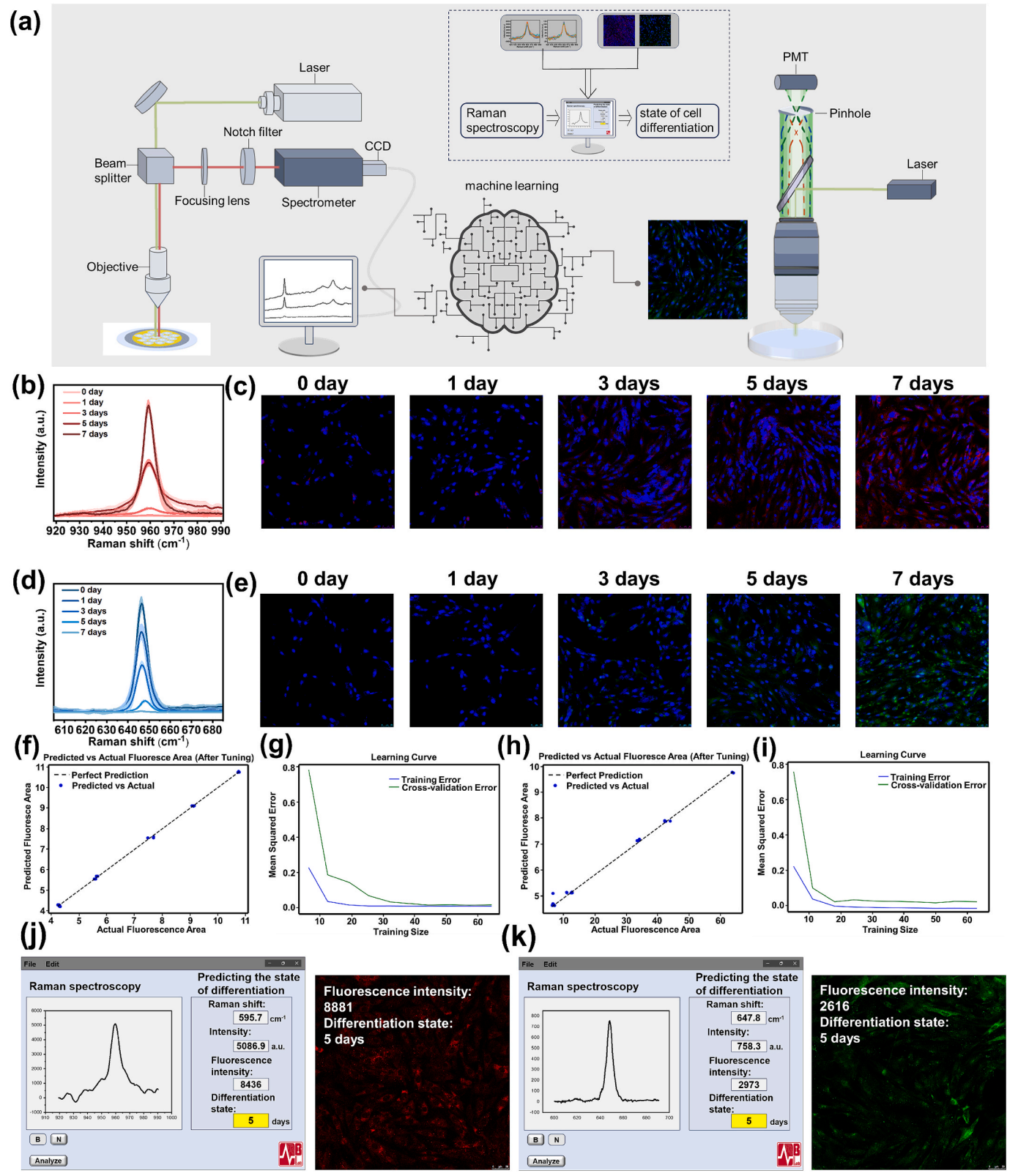

Fig. 6. Real-time prediction of cell differentiation via machine learning. (**a**) Schematic representation of real-time prediction of cell differentiation via machine learning. Average Raman spectra of different levels of differentiation of MSCs to (**b**) osteoblasts and (**d**) neuron-like cells. Examples of immunofluorescence staining of different levels of differentiation of MSCs to (**c**) osteoblasts and (**e**) neuron-like cells. The relationship between the actual and predicted fluorescence intensity based on a random forest regression model during the differentiation of MSCs to (**f**) osteoblasts and (**h**) neuron-like cells. Representation of training size of (**g**) osteoblasts and (**i**) neuron-like cells as a function of mean square error. Example demonstration of the prediction of MSCs differentiation to (**j**) osteoblasts and (**k**) neuron-like cells.

Real-time prediction of cell differentiation via AI

In a biological perspective, the process of cell differentiation is often accompanied by phenotypic changes, including alterations in morphology, molecular markers, and cellular behavior. Traditional statistical methods struggle to handle these high-dimensional, multimodal data. Currently, AI techniques, particularly machine learning and deep learning models, can effectively identify and predict different differentiation states of cells by leveraging large-scale experimental data and high-dimensional spectral features (Fig. 6a). This dynamic predictive capability allows machine learning not only to provide static predictions of differentiation states, but also to track the progression of cells from their initial state to full differentiation, enabling more precise predictions at specific time points.

In this system, to identify the spectral changes associated with differentiation, two characteristic peaks were selected: the peak at 646 cm^{-1}, corresponding to the tyrosine vibration, which exhibits the most significant alteration during the differentiation of MSCs into neural-like cells; the peak at 960 cm^{-1}, associated with phosphate, which undergoes substantial change during the differentiation of MSCs into osteoblasts. As shown in Fig. 6b-6e, the Raman spectra and the immunofluorescence staining images of MSCs differentiated towards osteoblasts and neural-like cells at various time points are collected and used to establish the modeling spectral set for machine learning. Then, the relationship between the Raman spectral features and differentiation states of cells was modeled using a Random Forest Regressor approach. To assess the performance of the optimized model, predictions were made on the test set, and the model's efficacy was evaluated through the reporting of mean squared error (MSE) and the coefficient of determination (R2) (Fig. 6f-6i). Subsequently, the algorithm was developed into an application software, and the results of detecting the differentiation process of MSCs towards neural-like cells and osteoblasts were evaluated. The detection results of the differentiation of MSCs into neural-like cells are shown in Fig. 6j. The Raman intensity is 5086.9 a.u., corresponding to a predicted differentiation state at the 5-day mark, which aligns with the immunofluorescence staining results. Similarly, the detection results of the differentiation of MSCs into osteoblasts are shown in Fig. 6k. The Raman intensity is 758.3 a.u., corresponding to a predicted differentiation state at the 5-day mark, which is also consistent with the immunofluorescence staining results. Hence, combining experimental data with machine learning algorithms, the differentiation process of cells can be monitored in situ.

The established model effectively integrates immunofluorescence staining data with Raman spectral signatures to construct a predictive framework capable of characterizing the differentiation states of MSCs. By leveraging machine learning algorithms, the model was trained to accurately map spectral features to known fluorescence-based differentiation markers, enabling reliable prediction of MSC differentiation into both neural-like and osteogenic lineages. This approach not only demonstrates the capacity for non-invasive, label-free analysis at the single-cell level but also highlights the model's extensibility. While the trained model can be extended to other differentiation lineages, its application faces several key limitations: (i) Lineage specificity: the model is inherently lineage-specific, as spectral markers and their characteristic directions differ significantly between cell types. (ii) Need for adaptation: retraining or transfer learning is essential when applying the model to new differentiation pathways due to substantial variations in marker expression dynamics and signal intensities. (iii) Potential feature overlap: feature overlap within Raman spectra across lineages may impair classification clarity without prior feature selection or dimensionality reduction. Based on the incorporation of new, lineage-specific data, our framework can be extendable to additional lineages in the future. We believe this modularity presents a flexible and scalable solution for real-time, label-free monitoring across a variety of differentiation contexts.

Conclusion

In this study, light-triggered multiphysics-coupled Schottky superstructure has been engineered to integrate electrical stimulation and real-time detection functionalities. Opo-mechanically triggered BTO piezoelectric polarization causes the BTO band edge at the Schottky junction interface to bend downward, resulting in a lower Schottky barrier, which provides favorable conditions for the directional migration of electrons from Au to BTO. Under the synergistic effect of opto-mechanical coupling-triggered piezoelectric polarization and Schottky energy barriers, free holes are generated to electrically stimulate mesenchymal stem cells. Simultaneously, the self-assembled Au NRs embedded within Schottky superstructure serve as an effective SERS substrate, enabling label-free, non-invasive qualitative analysis of cells via Raman spectroscopy. Moreover, AI technology was employed to model the relationship between the Raman spectral features and differentiation states of cells, facilitating non-invasive, single-cell level estimation of differentiation status. This study proposed a new strategy to accelerate electrical stimulation differentiation, and realized a real-time, non-invasive differentiation process monitoring platform through the synergistic coupling of light-triggered multiple physical fields. Looking to the future, an innovative stimulation method based on multi-physics coupled Schottky superstructure exhibits remarkable potential to revolutionize real-time cellular interrogation, precision tissue regeneration, and adaptive bioelectronic interfaces.

CRediT authorship contribution statement

Jianying Ji: Writing – original draft, Investigation, Data curation. **Jiaxuan Li:** Data curation. **Cong Liu:** Writing – review & editing, Supervision. **Yiqian Wang:** Data curation. **Yuan Xi:** Data curation. **Engui Wang:** Data curation. **Yijie Fan:** Data curation. **Yizhu Shan:** Data curation. **Lingling Xu:** Data curation. **Yuan Bai:** Data curation. **Xi Cui:** Data curation. **Longfei Li:** Data curation. **Dan Luo:** Writing – review & editing, Supervision. **Zhou Li:** Writing – review & editing, Supervision, Funding acquisition.

Declaration of competing interest

The authors declare that they have no known competing financial interests or personal relationships that could have appeared to influence the work reported in this paper.

Acknowledgements

National Key Research and Development Program of China (2022YFB3804700 to Z.L.)

National Natural Science Foundation of China (T2125003 and 81971770 to Z.L.; 52372174 to D.L.)

Natural Science Foundation of Beijing Municipality (L245015 to Z. L.)

Fundamental Research Funds for the Central Universities (EOEG6802X2 and E2E46806 to Z.L.)

Appendix A. Supplementary data

Supplementary data to this article can be found online at https://doi.org/10.1016/j.mattod.2025.08.003.

Data availability

The authors do not have permission to share data.

References

[1] J. Wang, et al., Nano Energy (2019) 65.

[2] M. Duque, G. Murillo, Nano Energy (2024) 128.
[3] Y. Gou, et al., Bioact. Mater. 34 (2024) 51.
[4] X. Yu, et al., Adv. Mater. 36 (2024) 21.
[5] Q. Du, et al., Chin. Sci. Bull. 69 (2024) 15.
[6] Z. Lv, et al., Adv. Funct. Mater. 34 (2023) 10.
[7] Z. Li, et al., Nat. Commun. 14 (2023) 1.
[8] H. Wu, et al., Adv. Funct. Mater. 34 (2023) 4.
[9] J. Meng, et al., Sci. Bull. 69 (9) (2024) 1342.
[10] H.-J. Yoon, S.-W. Kim, Joule 4 (7) (2020) 1398.
[11] Z. Li, et al., MRS Bull. 50 (4) (2025) 468.
[12] S. Liang, et al., Adv. Funct. Mater. 34 (2024) 52.
[13] C. Yang, et al., Nanomaterials 12 (2022) 24.
[14] Y. Cheng, et al., Nano Energy (2020) 69.
[15] W. Liu, X. Wang, Nano Energy (2023) 117.
[16] L. Jing, et al., Small 20 (2024) 40.
[17] L. Wang, et al., Nano Energy 60 (2019) 724.
[18] S. Horiuchi, et al., J. Mater. Chem. C 6 (17) (2018) 4714.
[19] T. Liu, et al., Nano Today (2023) 52.
[20] J. Ji, et al., Adv. NanoBiomed Res. 3 (2022) 1.
[21] L. Lefaix, et al., Adv. Sci. (Weinh) (2025) e2415028.
[22] Z. Li, et al., Micro 4 (4) (2024) 823.
[23] P. Wu, et al., Mil. Med. Res. 10 (2023) 1.
[24] Y. Bai, et al., MedMat 1 (1) (2024) 40.
[25] L. Zhao, et al., Nano-Micro Lett. 13 (2021) 1.
[26] H. You, et al., Nat. Commun. 13 (1) (2022) 6144.
[27] I.P. Pozdnyakov, et al., Chemosphere 293 (2022) 133573.
[28] Y. Peng, et al., Exploration 5 (3) (2025) 270016.
[29] P. Samuelsson, et al., Meas. Sci. Technol. 33 (2022) 5.
[30] W. Yu, et al., Appl. Catal. B (2022) 310.
[31] H. Yuan, et al., Appl. Catal. B (2022) 314.
[32] Y. Shi, et al., Adv. Energy Mater. 13 (2023) 13.
[33] R.C. Forsythe, et al., Chem. Rev. 121 (13) (2021) 7568.
[34] Y. Chen, et al., Adv. Sci. 9 (2022) 10.
[35] Y. Wang, et al., Adv. Mater. 35 (2023) 45.
[36] J. Xiong, et al., Fundam. Res. 3 (2023) 37.
[37] Y. Yu, et al., J. Am. Chem. Soc. 144 (33) (2022) 15314.
[38] F. Madzharova, et al., Chem. Soc. Rev. 46 (13) (2017) 3980.
[39] X. Qin, et al., ACS Nano 18 (2024) 22.
[40] X. Bi, et al., Cell Rep. Med. (2024).
[41] S. Tian, et al., Nat. Commun. 11 (2020) 1.
[42] B. Yan, et al., Int. J. Oral Sci. 17 (2025) 1.
[43] X. Chen, et al., Adv. Sci. 10 (2023) 21.
[44] Z. Zhang, et al., Adv. Mater. 28 (43) (2016) 9589.
[45] P. Li, et al., Adv. Mater. 28 (13) (2016) 2511.
[46] R. Gao, et al., Nat. Commun. 15 (2024) 1.
[47] L. Zhou, et al., J. Mater. Chem. B 10 (43) (2022) 8797.
[48] B. Xie, et al., Nano Energy (2025) 138.
[49] S.M. Damaraju, et al., Biomaterials 149 (2017) 51.
[50] S.J. Smith, et al., Analyst 142 (11) (2017) 1962.
[51] H.K. Chiang, et al., J. Raman Spectrosc. 40 (2009) 546.